Nanoscale

PAPER

View Article Online
View Journal

Cite this: DOI: 10.1039/d6nr00624h

Bridging molecular and nano-scale kinetic regimes in the crystallization of icosahedral gold nanoparticles

Raj Kumar Ramamoorthy, †[a,b] Rohan Parmar,†[c] Ezgi Yildirim, [a] Marie Brut, [d] Sylvain David,[c] Simon Cayez, [a] Nicolas Ratel-Ramond, [a] Pierre Roblin, [c] Fabien Delpech, [a] Isaac Rodríguez-Ruiz, [c] Lise-Marie Lacroix, [a,e] Sébastien Teychené *[c] and Guillaume Viau *[a]

A precise description of the nucleation and growth mechanisms of nanoparticles in solution addresses fundamental challenges, such as comparisons with classical models or establishing alternative ones. Ultimately, it should lead to a better understanding of the parameters that govern the particle size and properties. This study focuses on ultrasmall gold nanoparticles with an icosahedral structure, prepared by the reduction of $HAuCl_4$ with triethylsilane (TES) in a nonpolar solvent containing oleylamine (OY). The final particles have a constant size of 2 nm, regardless of the reaction rate varied by adjusting the TES concentration. A particularity of this synthesis lies in the nature of the precursor solution: the Au^{III} complexes are not free but form a suspension of 4 nm gold chloride clusters coordinated to OY. The reaction was monitored *in situ* through XAS and SAXS, enabling kinetic studies at both the molecular and nano-scales. The nucleation stage involves the initial Au^{III} clusters and stops upon their complete disappearance. Growth proceeds in two successive distinct stages: an initial rapid stage following first-order kinetics with respect to Au and TES and a subsequent slower stage that is zero-order for Au and first-order for TES. At the end of the 1st stage, intermediate particles of 1.6 nm diameter, corresponding to 3-shell icosahedra, are formed. The rate-determining step of the 2nd stage is the reduction of Au^{III} complexes adsorbed at the particle surface. The limited number of adsorption sites on the intermediate particles due to a dense ligand capping layer and/or the slow diffusion of TES through this layer may explain the very slow reaction rate of the 2nd step. The relative stability of the intermediate magic size clusters covered with a dense ligand shell explains the abruptness of the transition between the 1st and 2nd growth stages. In this system, nucleation and growth do not follow the classical mechanism, and LaMer's postulate for monodisperse systems can be ruled out. This study highlights the critical influences of the stability of intermediate clusters, specific to magic size polyhedra, on growth kinetics. It also emphasizes the importance of precisely characterizing the initial precursor solution to accurately describe the nucleation.

Received 12th February 2026,
Accepted 29th April 2026

DOI: 10.1039/d6nr00624h

rsc.li/nanoscale

Introduction

Creating unique nanostructures with controlled properties is essential for harnessing the full potential and unprecedented performance of nanotechnology.[1–4] Gold nanoparticles (NPs) are a perfect example of a system where varying the crystallization condition is an effective way to control their surface chemistry, as well as their optical and electronic properties, enabling applications in plasmonics,[5] theragnostic,[6] molecular imaging,[7] drug delivery,[8] transparent electronics,[9] strain gauges[10] or catalysis.[11,12] Depending on the nucleation and growth mechanisms, a diverse range of particles has been synthesized, exhibiting unusual morphologies such as ultra-thin nanowires,[13] nanoribbons[14] or bipyramids,[5] or crystallizing with atypical atomic structures that deviate significantly from the Au bulk fcc structure, such as ultrasmall nanoparticles with an icosahedral structure,[15] ultrathin nanowires with a tetrahedrally closed-packed structure[16] or a 4H hexagonal

[a]Univ Toulouse, INSA, CNRS, LPCNO, Toulouse, France.
E-mail: guillaume.viau@insa-toulouse.fr
[b]Nanoscale and Interface Science Laboratory, Department of Physics, Anna University, Chennai 600025, India
[c]Univ Toulouse, INP Toulouse, CNRS, LGC, Toulouse, France.
E-mail: sebastien.teychene@toulouse-inp.fr
[d]Univ Toulouse, CNRS, LAAS, Toulouse, France
[e]Institut Universitaire de France, IUF, Paris, France
†These authors contributed equally to the study.

structure in the case of nanoribbons.[14] Controlling the NP size, shape, and crystalline structure depends strongly on the control of the nucleation and growth steps. As a result, determining whether the crystallization follows a classical or non-classical pathway has become an increasingly important field of research. Several reviews have been devoted to this topic in the specific case of nanoparticles synthesized in the liquid phase.[17–19] In short, classical nucleation theory (CNT) considers that nuclei are created in solution in a single step, that their structure is identical to that of the final particle, and that their size is governed by the surface tension of the material, the supersaturation of the solution, and the temperature. In this framework, the LaMer model describes the formation of monodisperse particles through a short nucleation period that reduces the concentration of monomers below the critical concentration (supersaturation threshold) and through the separation of the nucleation and growth stages.[20–22] However, several examples clearly contradict the classical theory for various reasons. In the case of metal particles, alternative kinetic models involving an autocatalytic reaction, without any reference to the surface energy of the particles, have been proposed.[23,24] Several studies evidenced complex multi-step crystallization pathways,[25] in the case of gold,[26,27] palladium[28] or silver nanoparticles.[29] For metal oxides in aqueous media, like Fe_3O_4 (ref. 30) and YVO_4,[31,32] amorphous intermediates were reported as determining the final nanoparticle size and crystallinity.[32] Several examples also reported the formation of dense liquid intermediates in which the primary particles nucleate.[26,33] In the case of quantum dots or metallic nanoparticles prepared in polar or non-polar solvents, nanometer sized prenucleation clusters of precursors have been evidenced.[34–36]

In this context, fully understanding the crystallization pathway requires the development of *in situ* and time-resolved studies across different scales. This involves using techniques capable of probing nascent condensed matter phases, such as liquid-phase transmission electron microscopy[26,28,33] or small angle X-ray scattering[37–40] and whenever possible, complementing them with UV-visible and X-ray absorption spectroscopies to precisely characterize the intermediate species at both the molecular and meso-scales.[41] For the latter techniques, rapid reactions also require the use of flow devices, ranging from micro- to milli-fluidics, compatible with synchrotron facilities and enabling the capture of processes from very short reaction times through to the end of the reaction.[35,37,42]

The specificity of nanoparticle synthesis in organic solvents lies in the presence of ligands, whose primary role is to reduce the surface energy of the particles and introduce a steric stabilization of the final suspension.[43] In non-polar solvents, these capping agents include long chain acids, amines, phosphines or thiols. For such syntheses, several examples have reported an extended nucleation period, with significant overlap between nucleation and growth often accompanied by size focusing during the growth. This behaviour has been observed in both metal particles[44] and quantum dots.[45,46] All these observations stand in clear contradiction to the LaMer model. The influence of the ligand layer capping the particle surface is often mentioned to explain why, in such syntheses, smaller particles grow faster than larger ones.[44–46] The role of these molecules extends beyond the growth stage. Acting as complexing agents for the metal precursor, they can modulate the kinetics of reduction/condensation and, in some case, can also serve as reactants.[47,48]

In this study, we have chosen to study the crystallization kinetics of ultrasmall Au NPs with an icosahedral structure, obtained by the reduction with triethylsilane (TES) of Au^{III} dissolved in a solution of oleylamine (OY) in hexane. Hydrosilanes are a class of mild reducing agents that have been used to synthesize noble metal NPs in organic media, including ultrathin Au nanowires,[49,50] Au[15,51] and Ag NPs,[52] and Cu nanowires.[53] Their reactivity depends on the nature of the organic substituents, which induce electronic or steric effects.[42] In this study, TES was chosen due to its demonstrated effectiveness in synthesizing monodisperse icosahedral NPs with very high yield,[15,52] unlike other reducing agents such as sodium borohydride and aminoboranes, which form Au NPs crystallizing with the fcc structure.[37,38,43] Icosahedra are well-known to form magic size clusters (MSC).[54] The high stability of MSC can generate a high energy barrier for the addition of subsequent atomic layers, leading to discrete, shell-by-shell growth and, in the case of icosahedral MSC, can involve complex pathways.[54–56] At very small sizes, mechanisms involving the specific growth of MSC are therefore expected to dominate. This system could therefore serve as a model for highlighting the specific nucleation and growth mechanisms of such MSC in solution. An additional distinguishing feature of this synthesis, compared to classical organometallic approaches, is the use of a metal salt as the precursor, dissolved in a nonpolar solvent through complexation with OY. In the case of Au^{III} or Ag^{I} ions, it has been shown that the precursors are not isolated metal complexes coordinated by OY, but rather aggregates of such complexes, often referred to as pre-nucleation clusters.[34,35,52]

The objective of the study was to describe as accurately as possible the evolution of the medium at both the molecular and nanoscales, in particular to examine the role of the initial Au^{III} clusters in the nucleation stage and possible MSC intermediates in the growth stage. The initial clusters formed by the interaction of $\{Au^{III}Cl_4\}$ and OY in hexane are described first, using SAXS-WAXS, NMR and DFT calculations, followed by the characterization (SAXS, WAXS, NMR) of the final particles obtained through the reduction of these Au^{III} clusters with TES. We then present the kinetic studies conducted using X-ray absorption spectroscopy (XAS) and small angle X-ray scattering (SAXS). The reduction and crystallization of Au icosahedral NPs at different TES concentrations was monitored *in situ* using a microfluidic set-up. Combining XAS and SAXS, the $Au^{III}/Au^{I}/Au^{0}$ molecular speciation as well as the size and polydispersity of the scattering objects were determined throughout the reaction. A kinetic model is then proposed to account for the sequence of the two well-separated growth stages and the formation of an intermediate MSC observed experimentally. This model describes the transition between kinetic regimes at the molecular and nanoparticle scales.

Results and discussion

Au NPs were prepared by adding a solution of triethylsilane (TES) in hexane to a solution previously prepared by dissolving $HAuCl_4{\cdot}3H_2O$ in a solution of oleylamine (OY) in hexane. The TES and gold concentrations were varied but the molar ratio [OY]/[Au] was fixed to 2.5 in all experiments (see experimental details in SI section I). In this section, we first describe the precursor solutions, then the Au NP suspensions obtained after reduction.

From Au^{III} clusters to Au^0 nanoparticles

Characterization of the Au^{III}-OY precursor suspensions. The SAXS of the pale-yellow precursor solutions, before adding TES, exhibited a strong intensity with a plateau at small-q (Fig. 1a). This signal is attributed to the clustering in hexane of the Au^{III} ions coordinated by chloride anions and/or OY.[34,35] Such a scattering signal was observed throughout the gold concentration range of 1 to 20 mM, showing the presence of Au^{III} clusters even at the lowest concentrations. The SAXS profiles were fitted using a Guinier–Porod model with the scale factor (G), the porod exponent (m), the radius of gyration (R_g) and the dimensionality (s) of the scattering objects as adjustable parameters (SI, section II.1). In all cases, the best fits were obtained with $s = 0$ (spherical objects) and $m = 4$ (smooth interface). The diameter of the Au^{III} clusters was found to increase slightly from 3.6 to 4.2 nm when the Au concentration was increased

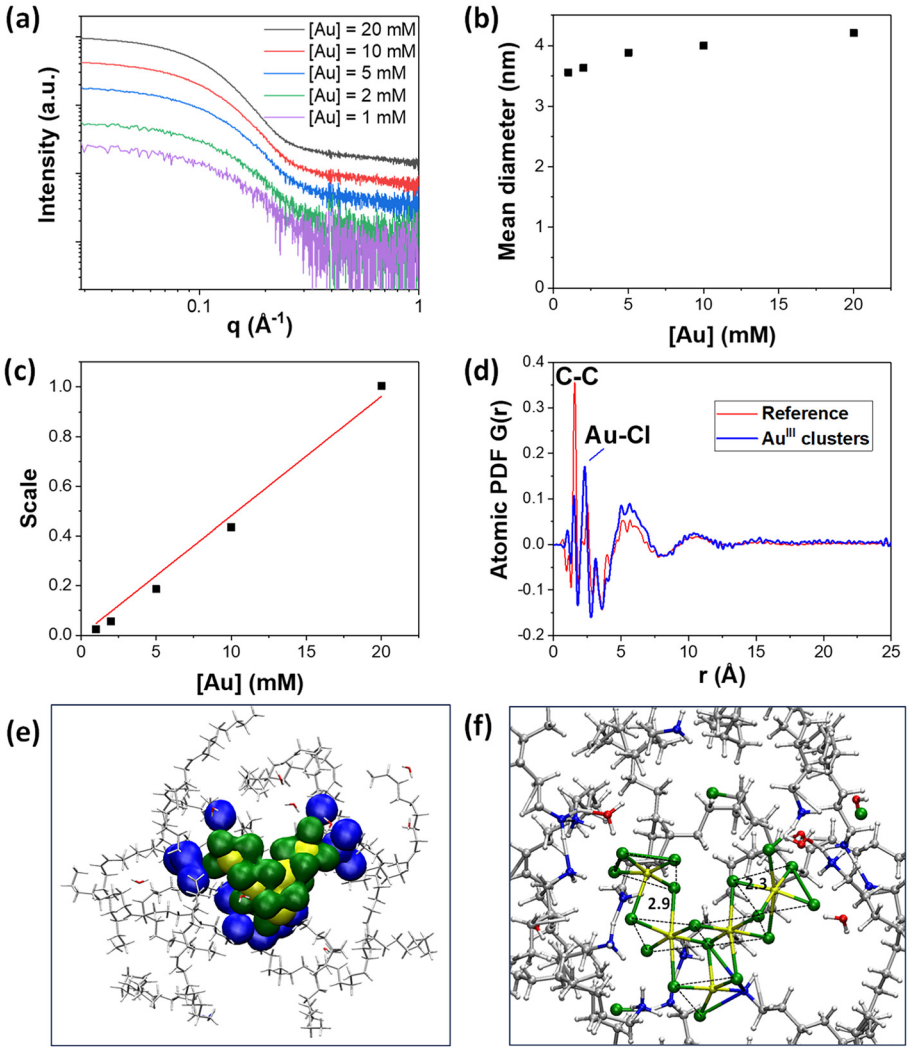

Fig. 1 Characterization of the Au^{III} precursor solution: (a) *in situ* SAXS at 25 °C of the Au^{III} clusters obtained by dissolution of $HAuCl_4{\cdot}3H_2O$ in a solution of oleylamine in hexane (the Au concentration was varied from 1 to 20 mM, the ratio OY/Au was kept constant at 0.25); (b) mean diameter of the Au^{III} clusters at different Au concentrations given by the fit of the SAXS with a Guinier–Porod model (see eqn (S1) in the SI) (s and m values were found to be constant and equal to 0 and 4, respectively); (c) scale values as a function of Au nominal concentration; (d) PDF of the Au^{III} precursor suspension (blue) compared to the PDF of oleylamine in hexane at the same concentration; (e) structure of a small Au^{III} cluster obtained by semi-empirical MD simulations showing a $AuCl_4$ core surrounded by a first shell of nitrogen atoms from oleylamine and oleylammonium and water molecules and an outer layer of alkyl chains from oleylamine and oleylammonium. Color code: red: O, white: H, blue: N, yellow: Au, green: Cl. (f) Atomistic view of the cluster in its environment. Dashes are used to visualize the square-planar $AuCl_4^-$ geometry. Au–Cl distances are indicated in Å.

from 1 to 20 mM (Fig. 1b). Interestingly, the scale factor values were found to increase linearly with the Au nominal concentration (Fig. 1c). Partial dissolution of the Au^{III} clusters at low concentration would have led to a deviation from this linear relationship. In the case of an equilibrium between Au^{III} complexes free in solution and involved in the clusters, the decrease of the Au nominal concentration would have led to a faster decrease of the SAXS signal at low concentration (SI, section II.2 and 3). The linear relationship in Fig. 1c shows that no free Au^{III} complex could be detected in solution. In the whole concentration range, the degree of dissociation of the Au^{III} clusters is very low, close to zero. We can therefore conclude the absence of isolated free Au^{III} ions in hexane despite the complexation with oleylamine.

The atomic PDF of the Au^{III} clusters shows no long-range order but rather a highly disordered/liquid like structure (Fig. 1d). The main difference between the PDF of the Au^{III} clusters and the reference of OY dissolved in hexane is the distance at 2.3 Å corresponding to the Au–Cl distance of the $\{Au^{III}Cl_4^-\}$ complexes, in agreement with previously reported EXAFS analysis.[35] The ^{1}H NMR spectrum of the precursor solution shows one broad resonance around 6.5 ppm (SI, Fig. S3) corresponding to the protons of the amino group of the oleylamine, of the ammonium group of the oleylammonium ions formed by the reaction with the proton of the gold precursor and of the water molecules coming from the gold precursor, involved in a fast exchange. The diffusion coefficient was inferred from DOSY experiments on different protons of the oleylamine (or oleylammonium) chains. The corresponding hydrodynamic diameter was found equal to 1.75 nm, much lower than the diameter deduced by SAXS. The NMR diameter corresponds to the average between free oleylamine and oleylammonium molecules and those coordinated to Au^{III} and involved in the clusters. The low diameter given by ^{1}H NMR is in good agreement with a fast exchange between the oleylamine and oleylammonium molecules in solution and the ones coordinated to Au^{III}.

To clarify the internal structure of the Au^{III} clusters, DFT calculations and semi-empirical molecular dynamics simulations were performed (computational details in SI, section III). These simulations reveal a gold–chloride core surrounded by a shell containing nitrogen atoms from oleylamine and oleylammonium ions. Within the core, most Au^{III} centers remain coordinated to four chloride ligands, while a minority adopts a three-chloride/one-nitrogen environment through interaction with oleylamine. The calculations also uncover a stable structural organization in which $AuCl_4^-$ units arrange so that their planes form the square bases of pyramidal or bipyramidal motifs, with the apex defined by a chloride ligand originating from an adjacent plane. Around this core, water molecules either diffuse freely or assemble into small clusters, while an outer layer of disordered alkyl chains from oleylamine and oleylammonium ions surrounds this assembly (Fig. 1e and f). Although the model includes a limited number of Au^{III} ions imposed by computational constraints, it provides a reliable small-scale representation of the clusters consistent with the experimental observations.

The precursor solution can therefore be described as a two-phase suspension with nanodroplets/clusters containing Au^{III} ions coordinated to Cl and oleylamine, in fast exchange with water molecules and ammonium, with the alkyl chains pointing toward the hexane solution containing free OY. Density measurements were performed to assess the scattering length density and the number of Au^{III} complexes contained in one cluster (SI, section II.4–6). Under the assumption that the core of the Au^{III} clusters is made up of aggregates of formula $\{AuCl_4{\cdot}3H_2O\}_n$, the average number of Au^{III} ions in one cluster, n, was found to be equal to *ca.* 100 for the nominal concentration [Au] = 20 mM and the scattering length density equal to 16×10^{-6} Å^{-2}, *i.e.* a little bit less than one order of magnitude than the sld of Au^0. Assuming 100 Au atoms per cluster, the number density of Au^{III} clusters was found to be equal to 12×10^{16} cm^{-3} for the gold concentration of 20 mM.

Reduction step and characterization of the final Au^0 NPs. A solution of TES in hexane was added to the Au^{III} cluster suspensions to reduce them into Au^0 NP suspensions. The color of the precursor solution turned from pale yellow to dark red brown rapidly after introducing the TES. The NP suspensions were characterized by TEM, *in situ* SAXS and NMR, 3 hours after the introduction of TES to ensure 100% yield of reduction. According to ^{29}Si NMR results (section I in SI) TES is transformed into triethylchlorosilane. The stoichiometry of the reduction of Au^{III} by TES is given by the following equation:

$$HAuCl_4 + \frac{3}{2}R_3SiH + \frac{5}{2}C_{18}H_{35}NH_2 \rightarrow Au(0) + \frac{3}{2}R_3SiCl + \frac{5}{2}C_{18}H_{35}NH_3{}^+Cl^-$$

The reduction of 1 eq. of Au^{III} requires 1.5 eq. of TES and releases 2.5 eq. of H^+ neutralized by 2.5 eq. of OY.

In the first set of experiments, the gold concentration was kept constant, [Au] = 20 mM, and the TES concentration was varied from a slight excess (62 mM) to a very large one (500 mM). A representative TEM image is given in Fig. 2a showing that the main population of NPs was isotropic NPs of diameter around 2 nm. The SAXS signal of the nanoparticles prepared with [TES] = 500 mM and the result of the fit are shown in the inset of Fig. 2b. The SAXS data of Au NP suspensions prepared with the other TES concentrations, from 62 mM to 250 mM, and the corresponding fits are given in Fig. S11 (SI). All the Au NP SAXS profiles were nicely fitted by a sum of two form factors of nanospheres, with the polydispersity being represented by a Schulz distribution for both cases. Table 1 shows the NP mean size and size distribution obtained from the fitting of the Au NP SAXS. The dominant population (pop. A) exhibited a mean diameter of 1.9–2.1 nm, remaining almost constant across the tested TES and Au concentration ranges (Fig. 2b). The smallest particles constituted more than 90% of the number fraction (except at the lowest [TES]), in line with the TEM images. The atomic structure of the Au^0 particles was analyzed by PDF calculated from the HE-XRD patterns recorded *in situ*. The structure was found to be icosahedral

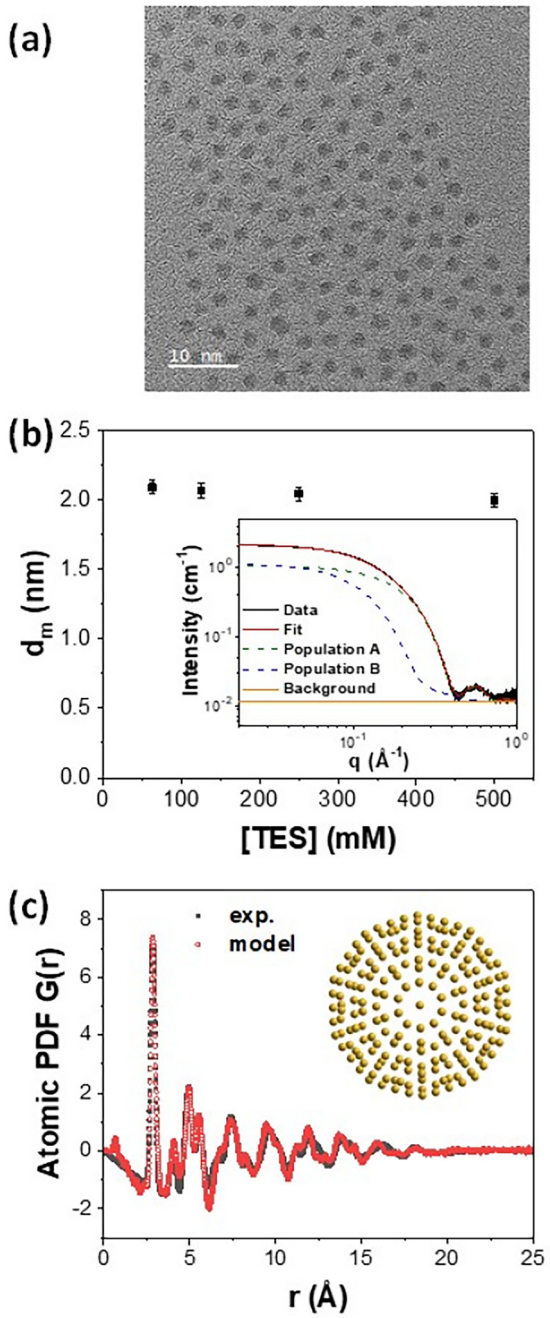

Fig. 2 (a) Representative TEM image of Au NPs prepared by reduction of the Au^{III} precursor solution with [TES] = 500 mM; (b) mean diameter of the major population of nanoparticles as a function of [TES] obtained by fitting the *in situ* SAXS. Inset: an example of SAXS analysis using two populations of spheres; (c) experimental atomic PDF of the particles prepared with [TES] = 125 mM (black) and calculated PDF of a 4-shells icosahedron model (red) represented as the inset.

regardless of the TES concentration used. The best fit was obtained with a 4-shell icosahedron model, in agreement with the particle size determined by SAXS (Fig. 2c and Fig. S13).

In the second set of experiment, [Au] was varied between 2 mM and 20 mM while [OY]/[Au] was fixed to 2.5 and [TES] was kept constant to 500 mM. The SAXS results, summarized in the SI (section IV), showed that the large majority of particles have a diameter close to 2 nm regardless of [Au] (Fig. S12). The total Au^0 concentration calculated from the volume fraction given by the SAXS fitting consistently matched the nominal value, confirming that the reduction yield was always 100% (Fig. S12d).

As the experimental conditions correspond to the stoichiometric proportions of the balance equation, all the oleylamine is converted into oleylammonium chloride at the end of the reaction. The final particles are stabilized by chloride and ammonium ions as shown experimentally by XPS[35] and confirmed theoretically by DFT calculations revealing that co-adsorption of both ions results in higher adsorption energy.[50] The hydrodynamic diameter of the Au NP calculated from the diffusion coefficient inferred from DOSY experiments on different protons of the oleylammonium chains was found to be equal to 3.65 nm. This diameter corresponds well to that of 2 nm gold nanoparticles coated with long-chain ligands (oleylammonium). This value also indicates that the ligands are strongly bound to the surface and are no longer in rapid exchange with the solution.

Summary. In conclusion of this first part, the dissolution of $HAuCl_4$ in a solution of oleylamine in hexane forms a suspension of gold chloride clusters coordinated with oleylammonium and oleylamine. These clusters contain approximately 100 molecular units. The reduction of these suspensions by TES yielded icosahedral NPs, the best model for which is the 4-shell icosahedron, *i.e.* containing 309 atoms. The overall chemical reaction can therefore be represented by the following equation:

$$3\{Au^{III}Cl_{4-x}^{-}(RNH_3^{+})_{(1-x)}(RNH_2)_x\}_{100} \rightarrow \{Au_{300}^{(0)} \cdot (Cl^{-}RNH_3^{+})_z\}$$

Surprisingly, the NP mean size was almost independent of [TES] and [Au]. Since the reaction rate is typically influenced by both concentrations, classical nucleation theory would predict a corresponding effect on the final particle size. To better understand the NP nucleation/growth process of the Au particles, kinetic studies of the nucleation and growth were carried out. These were done using a microfluidic set-up described in a previous paper.[42] The microreactors are composed of two injection inlets, one for the Au^{III} precursor suspension and the second one for the TES solution, a butterfly microfluidic mixer to ensure a fast and homogeneous mixing of the solutions, and an interrogation channel suitable for use with synchrotron radiation (Fig. S2). The chemical reaction was followed in continuous-flow configuration to have access to the short times (deriving reaction times as a function of microreactor length) with a resolution of 300 ms, and then in stopped flow configuration for the longer times. When the flow was stopped the reaction continued in the interrogation channel. The Au NP formation was monitored by XAS at the Au L_{III} edge and by SAXS, independently, on synchrotron beamlines.

Table 1 Values of the adjustable parameters of the two Schultz distributions (A and B) used to fit the experimental SAXS pattern of Au nanoparticle suspensions obtained after 3 h of reaction using TES at different concentrations with [Au] fixed at 20 mM and for different Au concentrations with [TES] fixed at 500 mM

		Population A				Population B			
[Au] (mM)	[TES] (mM)	R_m (Å)	σ/d_m	Vol%	% number	R_m (Å)	σ/d_m	Vol%	% number
20	62	10.5	0.05	71.3	85.6	14.0	0.20	28.7	14.4
20	125	10.3	0.05	77.5	90.3	14.4	0.20	22.5	9.7
20	250	10.2	0.05	81.5	93.0	14.8	0.21	18.5	7.0
20	500	10.0	0.05	82.3	94.0	15.0	0.19	17.7	6.0
2	500	9.8	0.1	86.5	95.6	16.7	0.15	13.5	4.4
5	500	10.3	0.09	84.4	93.6	17.3	0.14	15.6	6.4
10	500	10.3	0.09	86.9	95.3	17.8	0.14	13.1	4.7

dm is the mean diameter, σ/dm is the polydispersity ratio, vol% is the relative volume fraction of both populations and % number is the relative proportion of the number of particles for both populations.

Kinetic study by X-ray absorption spectroscopy

The time-resolved XAS spectra were fitted using a linear combination of three references for Au^{III}, Au^{I} and Au^{0} oxidation states measured at the Au L_{III} edge (Fig. S14). The relative weights of each component in the linear combination give the proportions of the different oxidation states. 100% represents the total Au concentration in the experiment, *i.e.* $[Au]_0$ = 20 mM. In the SI, two examples of XAS spectrum fitting are provided (Fig. S14b and c), along with the XAS spectra of the three Au^{III}, Au^{I} and Au^{0} references (Fig. S14d–f).

The time evolution of the normalized concentrations of Au^{III}, Au^{I} and Au^{0} during the first 500 seconds of NP synthesis, with [TES] ranging from 62 to 500 mM, is shown in Fig. 3 and S15. For all TES concentrations no induction time could be detected. Two distinct stages were clearly identified. A fast reduction characterized by a steep increase of $[Au^0]$ was observed first, then when $[Au^0]$ reached a value close to 0.6, regardless of [TES], a break in the kinetic regime was observed and the $[Au^0]$ increase became very slow (Fig. 3). The duration of both stages decreased as [TES] was increased, showing that the reduction rates of both stages increased with increasing [TES]. During the first stage, $[Au^I]$ decreased rapidly to 0 after reaching a maximum value, less than 20% of the nominal concentration when [TES] = 62 mM and even less than 10% with higher [TES]. During the second stage, the Au^I concentration was always zero showing that the reduction of Au^I to Au^0 is much faster than the reduction of Au^{III} to Au^I.

The time-dependences of $[Au^{III}]$ in Fig. 3 were analyzed in closer detail. The sum of an exponential decay and a linear decay (eqn (1)) was found to nicely fit the experimental data (green lines in Fig. 3 and S15):

$$[Au^{III}] = [Au^{III}]_{int} + (1 - [Au^{III}]_{int})\exp(-kt) - k't \quad (1)$$

The values of the three fitting parameters, k, k' and the intermediate concentration $[Au^{III}]_{int}$, are reported in Table S2 for the different [TES] values. The value of $[Au^{III}]_{int}$ was very close to 0.4, regardless of [TES].

A comparison of the exponential and the linear decays shows that the time dependence of $[Au^{III}]$ can be described by two successive stages well separated in time (Fig. S16). $[Au^{III}]$ decreases exponentially with time during the 1st stage (eqn (2)), followed by a second stage characterized by a linear decrease (eqn (3)). The critical times t_1^*, at which $[Au^{III}] = [Au^{III}]_{int}$ and t_2^*, at which the linear decay becomes faster than the exponential one, both decrease with increasing [TES] (Table S2 and Fig. S16 and 17).

$$[Au^{III}] = [Au^{III}]_{int} + (1 - [Au^{III}]_{int})\exp(-kt) \quad (2)$$

$$[Au^{III}] = [Au^{III}]_{int} - k't \quad (3)$$

The exponential decay shows that the order of the reaction is 1 with respect to Au^{III} during the first stage. The rate constant k, determined from the fit of this stage, was then plotted as a function of [TES] (Fig. 4). k is found to be proportional to [TES], indicating that the reaction order is also 1 with respect to TES. The reaction rate of the first stage is therefore described by eqn (4).

$$-\frac{d[Au^{III}]}{dt} = k_1[Au^{III}][TES] \quad (4)$$

Eqn (2) is the solution of eqn (4) for $k = k_1[TES]$ under boundary conditions $[Au^{III}] = 1$ at $t = 0$ and $[Au^{III}] = [Au^{III}]_{int}$ when $t \to \infty$. When TES is in large excess with respect to $[Au^{III}]$, the constant k_1 of eqn (4) is the slope of the linear variation of k with [TES] reported in Fig. 4. For [TES] values ranging from 125 to 500 mM, the calculated rate constant was found to be $k_1 = 3.05 \times 10^{-1}$ mol^{-1} L s^{-1}.

The linear decay observed during the second stage indicates that the reaction is zero-order with respect to Au^{III}. The k' value deduced from the fits was found to be proportional to [TES] (Fig. 4) showing a first-order with respect to TES. The reaction rate of the 2nd stage writes as:

$$-\frac{d[Au^{III}]}{dt} = k_2[TES] \quad (5)$$

Eqn (3) is the solution of eqn (5) under the boundary conditions $[Au^{III}] = [Au^{III}]_{int}$ for $t = 0$. For [TES] values ranging from 125 to 500 M, a value of $k_2 = 3.1 \times 10^{-3}$ mol^{-1} L s^{-1} was obtained when $[Au^{III}]_0$ was normalized to 1 and k' was

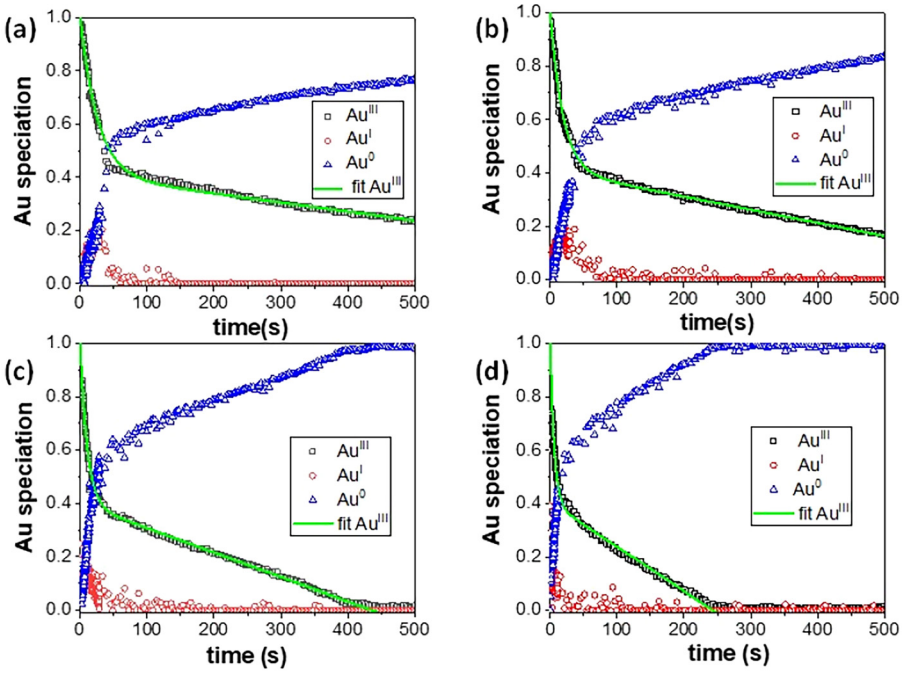

Fig. 3 Relative Au^{III}, Au^{I} and Au^{0} concentrations deduced from the linear combination analysis of the XAS spectra obtained *in situ* during the reaction with (a) [TES] = 62 mM; (b) [TES] = 125 mM; (c) [TES] = 250 mM; (d) [TES] = 500 mM. The green lines are the best fit of $[Au^{III}]$ using eqn (1) (see the text).

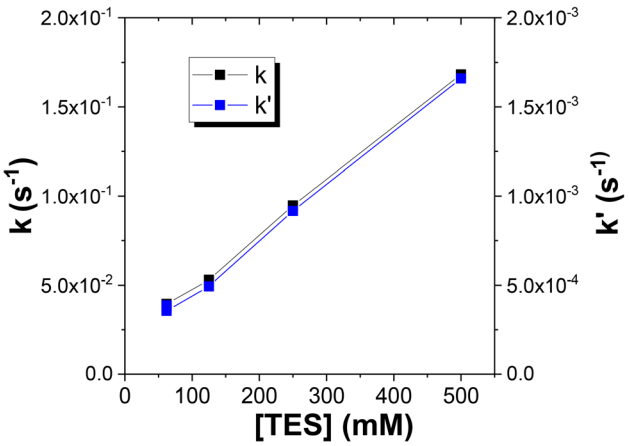

Fig. 4 *k* and *k'* constants, resulting from the best fits of the $[Au^{III}]$ curves with eqn (1), plotted as a function of [TES].

expressed in s^{-1} ($k_2 = 6.2 \times 10^{-5}$ s^{-1} when $[Au^{III}]_0$ is expressed in mol L^{-1}).

Kinetic study by SAXS

The same microfluidic set-up was used for time-resolved SAXS experiments. Fig. 5 shows an example of SAXS recorded for the concentrations [Au] = 20 mM, [OY] = 50 mM and [TES] = 125 mM. At short reaction times (Fig. 5a), a strong increase of the scattering intensity at high *q* values and a small increase of the plateau intensity at low *q* were observed. The high-*q* region modification can be interpreted as the onset and progressive increase of a form factor of particles smaller than the initial Au^{III} clusters. To highlight this point, the SAXS signal of the very first position in the channel, corresponding to a reaction time of 300 ms, was plotted and compared with that of the precursor suspension (Fig. S18). Notably, just 300 ms after addition of TES, the SAXS signal exhibits a shoulder at high *q*, whose intensity increases with [TES]. This shoulder indicates the presence of ultrasmall Au^{0} particles within the Au^{III} cluster precursor suspension. At short times, the SAXS transformation is related to the nucleation of Au^{0} NPs and the beginning of growth. At longer times (Fig. 5b) the main evolution of the SAXS patterns was the slow increase of the plateau intensity at low *q* which can be interpreted as a progressive increase in the size of the Au NPs. The fast variation of the SAXS signal at short times followed by a much more progressive evolution at longer times is in qualitative agreement with the time-resolved XAS data described in the previous section.

After approximately 800 s, no further variation was detected, showing that the reduction of Au^{III} to Au^{0} NPs was complete. The final SAXS were similar to those obtained from Au NPs prepared in vials (Fig. 2). They were nicely fitted by a sum of two nanosphere form factors, with the smaller NP constituting the main population, as previous described. The total Au NP volume fractions at the end of the reaction were found in the range of $2.1–2.2 \times 10^{-4}$, very close to the theoretical value of 2.04×10^{-4} calculated for the Au concentration of 20 mM.

At short times the scattering intensity results from a mixture of Au^{III} clusters and small Au^{0} NPs while at the end of

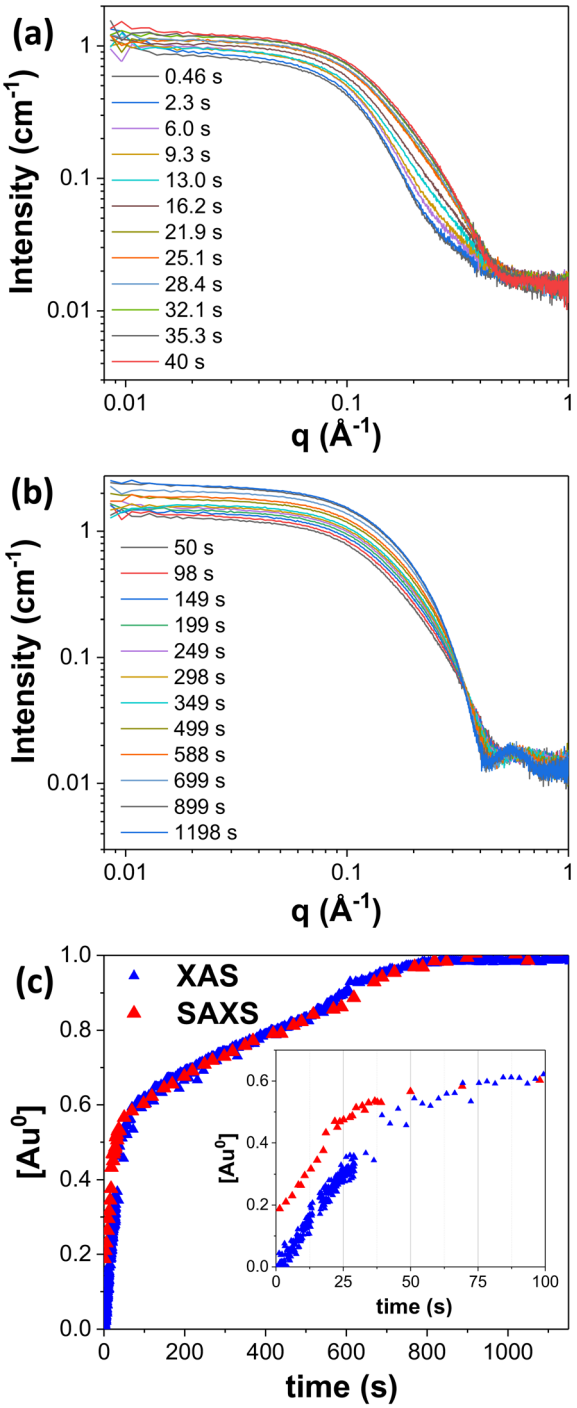

Fig. 5 (a and b) *In situ* SAXS recorded in microfluidics at increasing times during the reduction of a solution of $HAuCl_4{\cdot}3H_2O$ and oleylamine in hexane with triethylsilane ([Au] = 20 mM, [OY] = 50 mM, [TES] = 125 mM) (*t* = 0 corresponds to the introduction of TES); (c) comparison of [Au^0] given by the XAS and SAXS fitting considering a sum of two form factors of Au^0 nanospheres, showing an excellent agreement for the second stage and a discrepancy at short times. Inset: zoom on the first 100 s showing that after *ca.* 50 s the Au^{III} clusters initially present in the precursor suspension disappeared (see the text).

the reaction it comes from a mixture of small and large Au^0 NPs. Fitting accurately the SAXS data of the first stages of the reaction was challenging since three constituents could coexist in suspension, Au^{III} clusters together with small and big Au^0 NPs, that dramatically increased the number of fitting parameters. The fitting strategy therefore consisted of starting with the SAXS data at the end of the reaction and working backward in time. The SAXS curves were fitted with the sum of two form factors of nanospheres, denoted as population A and B. Population A refers to the smallest NPs in the reaction medium. These are the very first Au^0 NPs that appear at short times in the initial suspension of Au^{III} clusters. They then become the main population in the final suspensions. Population B refers to the largest particles in suspension. These particles can be the Au^{III} clusters present at short times or the biggest Au^0 NPs at longer times or a mixture of both for the intermediate time range. For the fitting at different reaction times, the sld of population A was chosen equal to the metal gold one, $sld_A = 118 \times 10^{-6}$ Å^{-2}, and the sld of population B was arbitrarily taken equal to the same value, $sld_B = 118 \times 10^{-6}$ Å^{-2}. The total gold concentration [Au^0] was calculated from the sum of the volume fractions of both populations. In the absence of Au^{III} clusters in the scattering intensity, [Au^0] given by the fits should correspond to the concentration determined by XAS. By contrast, a significant contribution of Au^{III} clusters to the scattering intensity at short times should reveal the differences in the [Au^0] values determined by the two methods. More details on the fitting procedure are given in the SI, section VII.

The normalized values of [Au^0] *vs.* time given by the XAS and SAXS fitting for [TES] = 125 mM are compared in Fig. 5c. The agreement between the two curves is excellent from *ca.* 50 s onwards and throughout the second stage of the reaction. It means that beyond 50 s the SAXS signal arises solely from Au^0 NPs. It shows that the contribution of Au^{III} clusters to the SAXS signal disappears at the end of the first stage. No more scattering Au^{III} clusters remain in suspension. After this time all residual Au^{III} precursors observed by XAS exist in the diluted molecular state. [Au^0] values derived from SAXS and XAS for the other TES concentrations are reported in Fig. S19, where an excellent agreement is also observed for the second reaction stage. The reaction end times determined by the two methods are almost identical. In contrast, a strong discrepancy between SAXS and XAS was observed during the first stage (inset of Fig. 5c and Fig. S19). At short times, the [Au^0] calculated from the SAXS fitting was overestimated because a significant contribution of the SAXS signal came from unreacted Au^{III} clusters still present in the reaction medium. This confirms that during the first stage, Au^{III} clusters gradually disappear and are no longer present at the onset of the second stage.

The second objective of the fits was to extract information on the size and number density of the different populations. As the biggest particles may correspond to Au^{III} clusters and/or to Au^0 NPs, the parameters determined for this population were not analyzed in detail thereafter. However, since the SAXS

signal of the smallest Au^0 NPs appears in a q-range strongly shifted relative to that of the biggest ones, the fitting results for the radius of population A and for its number density in the second stage of the reaction were considered reliable (SI, section VII). Fig. 6 shows the number density, radius and polydispersity of population A as a function of time for the experiment carried out with [TES] = 125 mM. The fast increase of ND_A observed at short times followed by its stabilization shows that nucleation stopped after *ca.* 75 s and the 2nd stage corresponds to the growth of a constant number of particles. Aggregation may occur during the first step (decrease in ND_A), but this hypothesis should be viewed with caution because, as mentioned above, the exact values of ND_A for the first step are not known with precision. The radius R_A increased steadily and rapidly during the first stage and much more slowly during the second stage after *ca.* 75 s (Fig. 6b). Additionally, the polydispersity of the population A, PD_A, steadily decreased throughout the growth stage (Fig. 6c).

Very similar conclusions were drawn from the fits of the time-resolved SAXS data performed at other TES concentrations (Fig. S20). The first stage corresponds to nucleation (increase in ND) and growth (increase in R) of gold nanoparticles. The time required for the ND to stabilize (end of nucleation) decreases with increasing [TES]. During the second stage, characterized by a constant number of particles, the growth rate (dR/dt) is much slower than during the first stage. Size focusing (decrease in PD) is observed in all cases (Fig. S20).

In addition, the critical radius (R_A^*), at which the change in growth regime occurs, is constant, ranging from 8 to 8.5 Å, regardless of [TES] (Fig. 6 and S20). During the second stage, the radius gradually increases from R_A^* to 10.5 Å. This corresponds to an increase of approximately one additional atomic shell. The SI includes the SAXS patterns of 3- and 4-shell icosahedra calculated using the Debye equation and fitted with a sphere form factor (Fig. S21). The resulting "SAXS radii" were 8.2 and 10.6 Å for the 3- and 4-shell models, respectively, very close to the experimental radii measured at the end of the first stage and at the end of the reaction, respectively. Thus, as a first approximation, we can consider that the end of the 1st stage corresponds to the stabilization of 3-shell icosahedra and that the 2nd stage corresponds to the growth of 3-shell icosahedra (147 atoms) into 4-shell icosahedra (309 atoms).

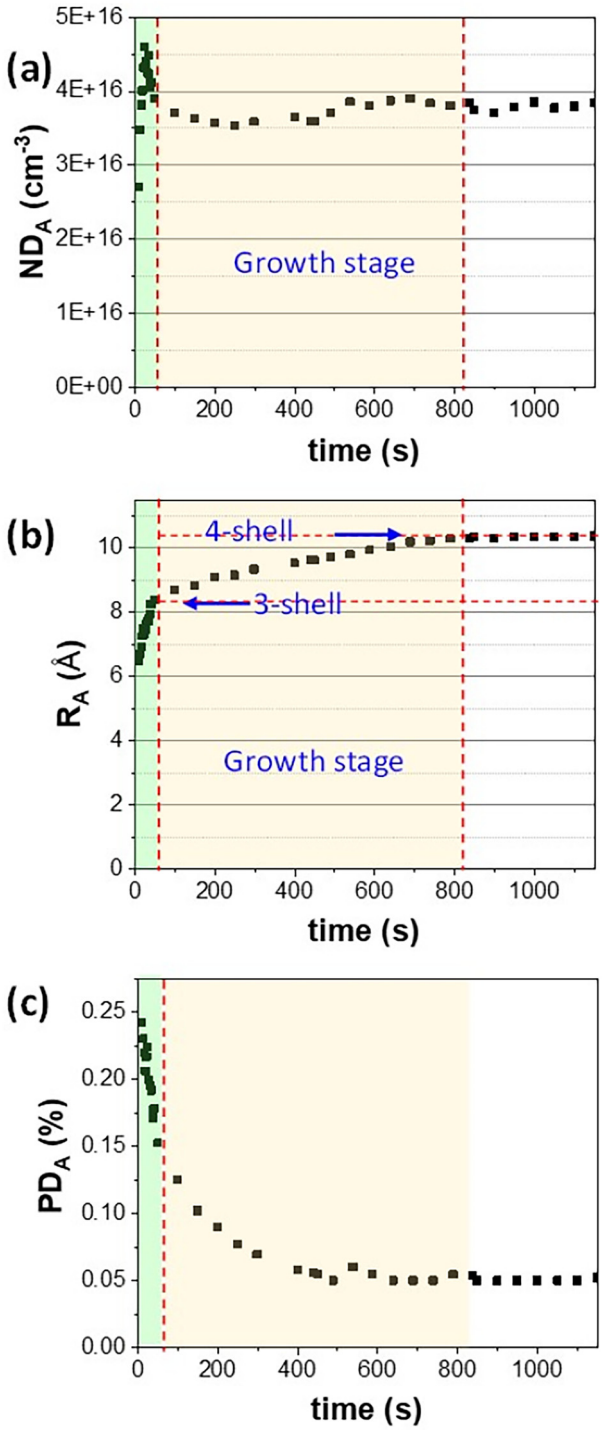

Fig. 6 Number density (a), mean radius (b) and polydispersity (c) of the major population of Au^0 NPs (smallest particles) as a function of time deduced from the SAXS fitting (reaction with [TES] = 125 mM).

Discussion on the nucleation and growth mechanism

The combination of XAS and SAXS techniques allows for accurate description of particle nucleation and growth, the former technique providing reaction rates and reaction order at the molecular level, the latter providing the number and size of particles during the reaction. Three points deserve to be discussed: (1) the role of the Au^{III} clusters in the nucleation step; (2) the zero-order reaction of the growth step; (3) the decrease in polydispersity during the growth stage.

Nucleation: the role of the Au^{III} clusters. In the classical nucleation mechanism, nucleation occurs when the monomer concentration reaches a critical value, the supersaturation threshold. At this point, the radius of the primary particles reaches a critical value and starts to grow. The nucleation rate depends on supersaturation, temperature and surface energy of the seeds, and in the case of atom-by-atom growth, the final particle size as well. In the framework of the classical nuclea-

tion theory, LaMer's model proposed that the formation of monodisperse particles is ensured by a clear separation between nucleation and growth steps: a short nucleation burst forms the nuclei and lowers the monomer concentration below the critical supersaturation threshold leading to the growth step without formation of additional nuclei.[20–22] In the examples reported here, some discrepancies with the LaMer model can be noted. The particle size increases significantly before the end of the nucleation stage, indicating that an overlap with growth is systematically observed (Fig. 6a and S19). Nucleation extends over different time periods depending on the experimental conditions without any influence on the particle size. No influence of the nominal Au concentration on the final particle size was observed, even when varied by an order of magnitude. Similarly, changing the overall reaction rate by adjusting [TES] did not impact the final particle size. The notion of a critical radius associated with a critical supersaturation as proposed by the classical nucleation theory seems to be called into question.

Initially, the Au^{III} precursor is exclusively incorporated into Au^{III} clusters, and nucleation stops when these Au^{III} clusters have disappeared. This strongly suggests that nucleation occurs within or at the surface of the Au^{III} clusters. However, the idea that one Au^{III} cluster would give rise to one particle is not consistent with the number density of each of the objects. According to the number densities of the initial Au^{III} clusters (*ca.* 12×10^{16} cm^{-3}) and of the final Au NPs (*ca.* 4×10^{16} cm^{-3}), we can conclude that around one-third of the Au^{III} clusters give rise to Au^0 primary particles. This suggests that a portion of the Au^{III} clusters is less reactive and/or the formation of the first primary Au^0 NPs modifies the organization of the Au^{III} complexes in suspension with the progressive disappearance of the Au^{III} clusters. Part of the initial Au^{III} clusters are also involved in the growth of the primary particles occurring during the first stage, since SAXS showed that the Au NP reached a diameter of about 1.6 nm at this stage, corresponding to a number of atoms greater than that of a single Au^{III} cluster.

The following sequence can be proposed: the first metal nuclei form within Au^{III} clusters and begin to grow. The Au^{III} clusters that have not reacted become unstable in the presence of the Au^0 nuclei. This instability may be due to an increase in the acidity of the solution, as oleylamine gradually converts to ammonium as the reaction proceeds. The resulting primary particles are surrounded by oleylammonium chloride arising from the reaction of OY with H^+ generated by the gold precursor and the reduction step (see the balanced chemical equation, section I) and by a diffuse shell of Au^{III} complexes coming from unreacted Au^{III} clusters. This shell acts both as a reservoir of precursors for the subsequent growth and as a capping layer that prevents the primary particles from agglomeration. The sharp transition between the first and second stages of the reaction can be attributed both to the end of nucleation and to the very slow growth rate of the last atomic shell. In the following section, additional arguments supporting this growth mechanism are presented.

Growth stage: the role of the ligand shell. It is noteworthy that once nucleation stops, the reaction order with respect to Au^{III} during the growth phase is zero. Measured by two independent techniques based on X-rays absorption and scattering, this result is highly reliable. Zero-order reactions are commonly observed in heterogeneous catalysis and surface chemistry. Surprisingly, they are extremely rare in the growth kinetics of nanoparticles. To the best of our knowledge, only one example has been reported so far, which described the growth of TiO_2-supported platinum nanoparticles.[57]

To rationalize the reaction orders observed during the growth only stage (second stage) a simple model based on an Eley–Rideal-type mechanism is proposed. Such a mechanism involves, first, the adsorption of Au^{III} complexes on sites located at the surface of primary Au NPs produced during the 1st stage (eqn (6)), followed by the reaction of TES with the adsorbed Au^{III} species (eqn (7) and (8)).

$$Au^{III}_{sol} + S \overset{k'_1}{\rightleftharpoons} Au^{III}_{ads} \quad (6)$$

$$Au^{III}_{ads} + TES \xrightarrow{k'_2} Au^{I}_{ads} \quad (7)$$

$$Au^{I}_{ads} + \frac{1}{2}TES \xrightarrow{k'_3} Au^0 \quad (8)$$

Au^{III}_{ads} denotes a reactive complex adsorbed at the surface of the primary NPs and Au^{III}_{sol} denotes a non-reactive complex not adsorbed at the primary NP surface. S denotes an unoccupied adsorption site and S_0 denotes the total concentration of adsorption sites on the NP surface.

$$S_0 = [Au^{III}_{ads}] + [S] \quad (9)$$

and $[Au^{III}_{ads}] = \theta S_0$ with θ is the fraction of occupied sites.

Throughout the second stage $[Au^I] = 0$ indicating that the reduction of Au^I to Au^0 (eqn (8)) is very fast compared to the reduction of Au^{III} (eqn (7)). The reaction in eqn (8) is thus absent from the expression of the reduction rate. If the surface reaction (eqn (7)) is the rate-determining step, *i.e.* if the equilibrium of eqn (6) is much faster than the reduction step, the reaction rate can be expressed as follows (see SI, section VIII, for more details):

$$-\frac{d[Au^{III}]}{dt} = \frac{d[Au^0]}{dt} = k'_2[TES]S_0 \times \frac{\frac{k'_1}{k'_{-1}}[Au^{III}_{sol}]}{1 + \frac{k'_1}{k'_{-1}}[Au^{III}_{sol}]} \quad (10)$$

If $[S] \ll [Au^{III}_{ads}]$, the proportion of unoccupied sites is very low (the surface sites are saturated by adsorbed Au^{III} species), then $1 \ll \frac{k_1}{k_{-1}}[Au^{III}_{sol}]$ and the reaction rate can be expressed as:

$$-\frac{d[Au^{III}]}{dt} = k'_2[TES]S_0 \quad (11)$$

Under these conditions, the reaction is zero-order with respect to Au^{III} and first-order with respect to TES. According to this model, the slope of the linear variation of k' with [TES]

reported in Fig. 3 is $k_2 = k'_2 S_0 = 3.1 \times 10^{-3}$ mol^{-1} L s^{-1}. Assuming that the kinetic constant k'_2 is equal to the kinetic constant of the first stage, k_1, we obtain an S_0 value of 1%, *i.e.* a concentration of 0.2 mM, corresponding approximately to 3 adsorption sites per particle if we consider that the nominal concentration of 20 mM is distributed over an ensemble of particles containing around 300 atoms each (2 nm icosahedra). This value is very low and may reflect the fact that the primary particles are covered by a dense layer of oleylammonium chloride, leaving little room for adsorption sites. Depending on the actual value of k'_2, S_0 could be higher but the global picture is that the low growth rate is linked to a low density of adsorption sites. This is consistent with NMR results showing strong adsorption of ligands on the NPs. The validity of the model assumes that S_0 remains constant during the growth stage. This is likely the case, as growth during the second stage involves only the addition of a single atomic layer, with little variation in the proportion of surface atoms. Notably, the linear regime was observed up to the very end of the reaction (Fig. 3), even when [Au^{III}] became very small, implying that the ratio k'_1/k'_{-1} is very large. Regardless of the concentration of Au^{III}, the fraction of unoccupied sites at the NP surface is always extremely low, with θ always remaining close to 1 till the end of the reaction. This can be attributed to a small number of adsorption sites and a very low solubility of the Au^{III} complex in hexane, as mentioned in the first section.

The kinetic analysis above relies on the implicit assumption that TES is readily available at the nanoparticle surface. A slightly different mechanism could also be considered in which the delivery of TES to the particle surface becomes rate-limiting. In this case, the reduction of adsorbed Au^{III} remains fast, but the overall growth rate is controlled by the transport of TES from the solution to the nanoparticle surface. Eqn (7) can be divided into two elementary reactions: the diffusion of TES from the solution to the particle surface (eqn (7a)) and the reaction of TES with adsorbed Au^{III} ions (eqn (7b)):

$$TES_{sol} \xrightarrow{k_d} TES_{surf} \quad (7a)$$

$$Au^{III}_{ads} + TES_{surf} \xrightarrow{k'_2} Au^{I}_{ads} \quad (7b)$$

If the diffusion of TES is the limiting step, the reaction rate can be expressed as follows (see SI, section VIII):

$$-\frac{d[Au^{III}_{tot}]}{dt} = k_d[TES_{sol}] \quad (12)$$

with

$$k_d = N_p 4\pi D \frac{Rr}{R-r} \quad (13)$$

where N_p is the particle concentration, D is the diffusion coefficient of TES, r is the nanoparticle radius and R is the capture radius. Under these conditions, the reaction is also zero-order with respect to Au^{III} and first-order with respect to TES. However, the rate constant determined by taking the diffusion coefficient of TES in hexane is several orders of magnitude higher than the experimental value k_2 (SI, section VIII). The growth regime limited by the diffusion of TES is not realistic unless TES diffusion is significantly reduced in the reaction medium. This alternative would thus stand only if the diffusion of TES through the ligand layer capping the particles is strongly hindered and the effective diffusion coefficient is of several orders of magnitude lower than that in pure hexane. A reaction limited both by the weak number of adsorption sites at the surface of the particles and by a very slow diffusion of TES to the particle surface cannot be completely excluded, but would require more precise knowledge of the effective diffusion constant of TES through a dense layer of ligands.

Size focusing. Finally, it is worth commenting on the decrease in polydispersity observed experimentally. Focusing or broadening of the size distribution during the growth stage strongly depends on the growth mode. The classic description of particle growth in solution distinguishes between the diffusion of the monomer from the solution to the particle surface and the incorporation of the monomer into the particle (surface reaction).[21] Size focusing is most favorable when diffusion is the rate-limiting step, as all particles, regardless of size, receive monomers at a similar rate resulting in a faster growth of the smallest particles. In contrast, when the surface reaction is rate-determining, larger particles, with a greater surface area, tend to grow faster than smaller ones, typically leading to size broadening. For growth of NPs in the liquid phase, based on diffusion coefficient values, it is commonly accepted that the surface reaction is the rate-determining step.[37,38] Despite this, several examples of liquid-phase synthesis of metal nanoparticles or quantum dots with size focusing observed during growth are reported in the literature.[24,44–46,58] Size-dependent ligand coverage of the NP surface, resulting in a reduced number of active sites as the particle size increases, combined with a deactivation of these sites, has been proposed to explain the size focusing of Pd NPs.[44] The role of the ligand shell at the surface of the nanoparticles has also been proposed as a key factor in explaining the size focusing. When diffusion through the ligand shell coordinated to the surface of the particles is the rate-determining step, the kinetics can be modeled similarly to diffusion-limited growth with the diffusion coefficient determined by the properties of the ligand shell, resulting in a growth regime that promotes size focusing.[45] The main features of the growth model proposed in the previous section, *i.e.* reduction at the surface as the rate-determining step, a strong dependence on the ligand adsorption on the particle size, and diffusion of TES limited by a dense layer of ligands, are consistent with these previous models.

One additional explanation for the decrease in polydispersity lies in the icosahedral structure of the NPs. For such a polymorph, theoretical calculations in a vacuum showed magic size clusters corresponding to deep energy minima. The growth of one additional shell on these MSC requires overcoming high energy barriers corresponding to high energy intermediate structures[56] and/or involving complex growth requiring concerted motion of many atoms of the growing shell.[54]

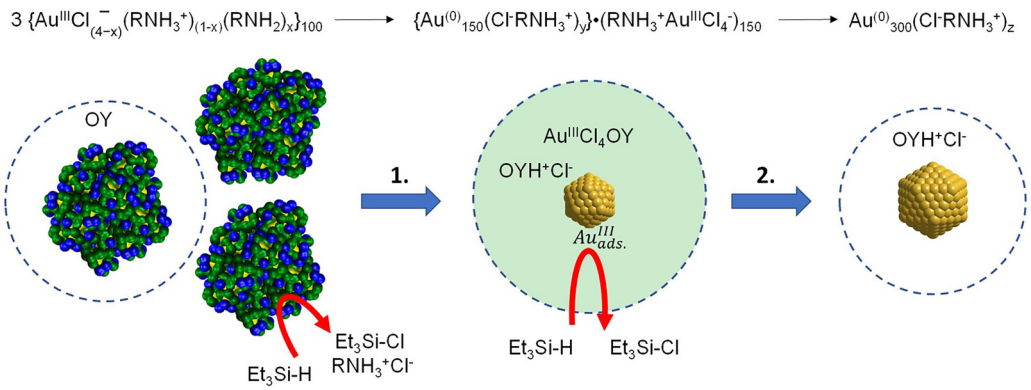

Fig. 7 Schematic of the different steps of the Au NP formation by reduction of {Au^{III}} clusters with TES (Et_3Si-H) in the presence of OY (RNH_2). Stage 1a: diffusion of TES inside Au^{III} initial clusters and Au^0 nucleation in some clusters. This step produces also oleylammonium chloride ion pairs that partially remain adsorbed at the surface of the Au^0 primary particles. Stage 1b: the formation of primary Au^0 NPs and the change in the medium composition cause a re-organization of the medium with the disappearance of the initial Au^{III} clusters and Au^{III} complexes adsorbed at the surface of the primary Au^0 NPs. Stage 2: at the end of the 1st stage, the resulting objects are on average 3-shell icosahedra capped with the first shell of oleylammonium chloride and adsorbed Au^{III} species, and a diffuse shell of Au^{III} complexes. The growth stage involves chemisorbed ions on the surface of the particles and diffusion of TES through the capping layer.

Here, the crystallization of intermediate 3-shell icosahedra combined with a full coverage of the surface with the ligand slowing down significantly the growth rate to reach the final 4-shell icosahedra may be responsible for a significant size focusing. The stability of intermediate 3-shell icosahedra covered by a dense layer of ligands could also explain the abruptness of the transition between the 1st and the 2nd stages.

Summary. Fig. 7 presents a schematic of the two reaction stages, summarizing the results obtained from XAS and SAXS. Two stages clearly separated in time and with different kinetics have been identified:

- The first stage is more complex than a simple reduction of free monomers in solution, as the dissolution of $HAuCl_4$ in a solution of OY in hexane leads to the formation of Au^{III} clusters, which serve as the true precursors of the gold NPs. The nucleation involves these 4 nm Au^{III} clusters and clearly stops upon their disappearance;

- The first-order reaction with respect to both TES and Au^{III} during this stage is characteristic of a molecular regime. It can be explained by the ability of TES molecules to diffuse inside the clusters and react with the Au^{III} complexes. This is consistent with the absence of a clear separation between the Au^{III} cluster shell and the solvent with a fast exchange of oleylamine and oleylammonium molecules between the initial clusters and the solution as shown by ^1H NMR;

- When the primary Au^0 NPs reach a size of 1.6 nm (3-shell icosahedra), regardless of the reaction rate, the growth regime changes completely. It is now governed by the surface chemistry of nanoparticles. The capping of intermediate 3-shell icosahedra with a dense oleylammonium chloride drastically reduces the number of adsorption sites available at the surface of the particles for the remaining Au^{III} complexes and limits the diffusion of TES. The reduction of adsorbed Au^{III} and/or diffusion of TES, as the rate determining step, explain the zero-order reaction for Au^{III} and a first-order reaction for TES. The second stage is very slow with respect to the first, consistent with the growth of a complete shell of magic sized icosahedral NPs (3-shell to 4-shell icosahedra) and a slow diffusion of the reducing agent across the ligand shell.

- The average number of Au^{III} complexes per cluster is estimated to be around 100, while the average number of Au atoms in the final particles is around 300 (4-shell icosahedral NP), indicating that only *ca.* 1/3 of the Au^{III} clusters are involved in the nucleation. Growth of the primary NPs occurs concurrently with nucleation during the first stage, resulting in 60% of Au^{III} consumed during this stage;

- One hypothesis for the absence of nucleation during the second stage is the reorganization of the medium driven by the increasing concentration of oleylammonium chloride and its transfer from the Au^{III} clusters to the surface of the metal particles. The Au^{3+} complexes no longer exist as dense clusters but form a diffuse layer on the surface of the metal particles (Fig. 7).

Conclusion

The syntheses studied in this article constitute a model system because they produce Au NPs whose mean size does not depend on the reaction rate, with a very narrow size distribution and an icosahedral structure. This is the first time that a kinetic study of crystallization of icosahedral NP in the liquid phase is reported in such detail. It highlights the critical influence of both the capping layer and the stability of intermediate magic size clusters on the kinetics of the growth stage. The role of intermediate magic-size clusters in the growth has been postulated but only very few studies have clearly identified their involvement in the growth mechanism.

What is particularly interesting in the present system is the sequential occurrence of two clearly separated steps: the first is well described by a first-order reaction with respect to both Au and TES, while the second corresponds to a zero-order reaction with respect to Au and a first-order reaction with respect to TES. Such a kinetic regime for the nucleation and growth of metal particles in solution has never been described before. A nucleation within clusters of the Au^{III} precursor, followed by the formation of primary particles embedded in a shell of Au^{III}, OY, and oleylammonium chloride, along with the slow reduction of Au^{III} complexes adsorbed on the seed surfaces, explains the kinetics of this reaction. Our explanation for the abruptness of the change in the kinetic regime is the formation during the first stage of intermediate particles of 1.6 nm diameter, corresponding to 3-shell icosahedra, embedded in a diffuse shell of Au^{III} complexes formed after nucleation, partial growth and oleylammonium chloride capping. At the end of this stage, the reaction rate becomes suddenly very slow because the primary 3-shell icosahedra are stable intermediate particles (magic sized icosahedra coated with a dense ligand layer) and the density of accessible adsorption sites is very low.

This study provides a new example of the importance to consider the versatile role of ligands at the different steps of the reduction to understand their role in the nucleation and growth of nanoparticles. This type of kinetic study could be easily extended to other metals. For example, the reduction of Ag^{I} is a promising system, as the reduction of silver nitrate by TES also yields icosahedral particles.[52] Such a study could offer further insights by examining the role of the Ag^{I}-OY clusters formed in hexane in the nucleation step. More broadly, deciphering this particular nucleation/growth mechanism provides wide perspectives on designing new syntheses based on the same strategic framework.

Author contributions

Conceptualization: R. K. R., I. R. R., L. M. L., S. T., and G. V. Data curation: R. K. R., R. P., E. Y., M. B., S. C., N. R-R., and F. D. Formal analysis: R. K. R., R. P., E. Y., M. B., N. R-R., F. D., S. T., and G. V. Funding acquisition: I. R. R., L. M. L., S. T., and G. V. Investigation: R. K. R., R. P., E. Y., M. B., S. D., F. D., P. R., I. R. R., L. M. L., S. T., and G. V. Methodology: R. K. R., R. P., E. Y., M. B., S. D., S. C., N. R-R., F. D., P. R., I. R. R., L. M. L., S. T., and G. V. Project administration: R. K. R., S T., and G. V. Resources: R. K. R., R. P., E. Y., M. B., S. C., N. R-R., F. D., P. R., I. R. R., L. M. L., S. T., and G. V. Software: R. K. R., M. B., S. C., and N. R-R. Supervision: R. K. R., I. R. R., L. M. L., S. T., and G. V. Validation: R. K. R., R. P., M. B., F. D., I. R. R., L. M. L., S. T., and G. V. Visualization and writing – original draft: R. K. R., R. P., M. B., F. D., and G. V. Writing – review & editing: R. K. R., R. P., M. B., I. R. R., L. M. L., S. T., and G. V.

Conflicts of interest

There are no conflicts to declare.

Data availability

All data supporting the findings of this study, including XAS, SAXS, NMR, and DFT calculations and semi-empirical molecular dynamics simulations, are provided in the 30 pages of the supplementary information (SI). Raw data analyzed during the current study are available from the corresponding authors upon request.

Supplementary information (30 pages, 21 additional figures): I. Experimental section; II. Analysis of the precursor suspensions – Characterization of the Au^{III} clusters; III. Atomic-scale simulations of the Au^{III} clusters; IV. SAXS analysis of the Au nanoparticles; V. Atomic structure – PDF analysis; VI. Time-resolved XAS analysis; VII. Time-resolved SAXS analysis; VIII. Kinetic modelling of the 2nd stage. See DOI: https://doi.org/10.1039/d6nr00624h.

Acknowledgements

This project has received funding from the French ANR competitive national call (Project NIMRod ANR-21-CE09-0019-01). R. P. thanks the EUR NanoX, n° ANR-17-EURE-0009, for funding for the HERCULES school. XAS experiments were performed on the beamline SuperXAS at SLS, PSI. SAXS experiments were performed on the beamline SWING at the French synchrotron Soleil proposal (proposal numbers: 20220441 and 20240444). Thomas Bizien and Javier Perez are warmly thanked for their assistance provided for the use of the beamline. XRD experiments were performed on the beamline ID15A at the European Synchrotron Radiation Facility (ESRF), Grenoble, France, proposal CH-6071. Stefano Checchia is warmly thanked for his assistance provided for the use of the beamline.

References

1 Y.-Z. Zhu, R.-Y. Zhou, S. Hu, J.-F. Li and Z.-Q. Tian, *ACS Nano*, 2024, **18**, 32287–32298.
2 F. Fioravanti, L. A. Pérez, G. I. Lacconi and F. J. Ibañez, *Langmuir*, 2025, **41**, 10408–10415.
3 S. Kinge, M. Crego-Calama and D. N. Reinhoudt, *ChemPhysChem*, 2008, **9**, 20–42.
4 J. F. Li, Y. F. Huang, Y. Ding, Z. L. Yang, S. B. Li, X. S. Zhou, F. R. Fan, W. Zhang, Z. Y. Zhou, D. Y. Wu, B. Ren, Z. L. Wang and Z. Q. Tian, *Nature*, 2010, **464**, 392–395.
5 J. Marcone, S. Juergensen, J. Barrios-Capuchino, X. Li, C. Goldmann, A. Köppen, W. Pfeiffer, F. Lehmkühler, W. J. Parak, M. Kociak, M. Impéror-Clerc, S. Reich, C. Hamon and F. Schulz, *Small*, 2025, **21**, 2500389.
6 M. A. Dheyab, A. A. Aziz, P. M. Khaniabadi, M. S. Jameel, N. Oladzadabbasabadi, S. A. Mohammed, R. S. Abdullah and B. Mehrdel, *Int. J. Mol. Sci.*, 2022, **23**, 7400.
7 M. Bouché, J. C. Hsu, Y. C. Dong, J. Kim, K. Taing and D. P. Cormode, *Bioconjugate Chem.*, 2020, **31**, 303–314.

8 F.-Y. Kong, J.-W. Zhang, R.-F. Li, Z.-X. Wang, W.-J. Wang and W. Wang, *Molecules*, 2017, **22**, 1445.
9 J. H. M. Maurer, L. González-García, B. Reiser, I. Kanelidis and T. Kraus, *Nano Lett.*, 2016, **16**, 2921–2925.
10 N. M. Sangeetha, N. Decorde, B. Viallet, G. Viau and L. Ressier, *J. Phys. Chem. C*, 2013, **117**, 1935–1940.
11 S. Peng, Y. Lee, C. Wang, H. Yin, S. Dai and S. Sun, *Nano Res.*, 2008, **1**, 229–234.
12 Y. Mikami, A. Dhakshinamoorthy, M. Alvaro and H. García, *Catal. Sci. Technol.*, 2013, **3**, 58–69.
13 A. Loubat, M. Impéror-Clerc, B. Pansu, F. Meneau, B. Raquet, G. Viau and L.-M. Lacroix, *Langmuir*, 2014, **30**, 4005–4012.
14 Z. Fan, M. Bosman, X. Huang, D. Huang, Y. Yu, K. P. Ong, Y. A. Akimov, L. Wu, B. Li, J. Wu, Y. Huang, Q. Liu, C. E. Png, C. L. Gan, P. Yang and H. Zhang, *Nat. Commun.*, 2015, **6**, 7684.
15 E. Yildirim, R. K. Ramamoorthy, R. Parmar, P. Roblin, J. A. Vargas, V. Petkov, A. Diaz, S. Checchia, I. Rodríguez-Ruiz, S. Teychené, L.-M. Lacroix and G. Viau, *J. Phys. Chem. C*, 2023, **127**, 3047–3058.
16 J. A. Vargas, V. Petkov, E. S. Nouh, R. K. Ramamoorthy, L.-M. Lacroix, R. Poteau, G. Viau, P. Lecante and R. Arenal, *ACS Nano*, 2018, **12**, 9521–9531.
17 N. T. K. Thanh, N. Maclean and S. Mahiddine, *Chem. Rev.*, 2014, **114**, 7610–7630.
18 J. Lee, J. Yang, S. G. Kwon and T. Hyeon, *Nat. Rev. Mater.*, 2016, **1**, 16034.
19 C. B. Whitehead, S. Özkar and R. G. Finke, *Mater. Adv.*, 2021, **2**, 186.
20 V. K. LaMer and R. H. Dinegar, *J. Am. Chem. Soc.*, 1950, **72**, 4847–4854.
21 T. Sugimoto, *Adv. Colloid Interface Sci.*, 1987, **28**, 65–108.
22 D. B. K. Chu, J. S. Owen and B. Peters, *J. Phys. Chem. A*, 2017, **121**, 7511–7517.
23 M. A. Watzky and R. G. Finke, *J. Am. Chem. Soc.*, 1997, **119**, 10382–10400.
24 D. R. Handwerk, P. D. Shipman, C. B. Whitehead, S. Özkar and R. G. Finke, *J. Am. Chem. Soc.*, 2019, **141**, 15827–15839.
25 P. G. Vekilov, *Nanoscale*, 2010, **2**, 2346–2357.
26 N. D. Loh, S. Sen, M. Bosman, S. F. Tan, J. Zhong, C. A. Nijhuis, P. Král, P. Matsudaira and U. Mirsaidov, *Nat. Chem.*, 2017, **9**, 77–82.
27 Y. Mikhlin, A. Karacharov, M. Likhatski, T. Podlipskaya, Y. Zubavichus, A. Veligzhanin and V. Zaikovski, *J. Colloid Interface Sci.*, 2011, **362**, 330–336.
28 W. Dachraoui and R. Erni, *Chem. Mater.*, 2023, **35**, 1201–1208.
29 J. Sun, B. Fritsch, A. Körner, M. Taherkhani, C. Park, M. Wang, A. Hutzler and T. J. Woehl, *Small Struct.*, 2024, **5**, 2400146.
30 J. Baumgartner, R. K. Ramamoorthy, A. P. Freitas, M.-A. Neouze, M. Bennet, D. Faivre and D. Carriere, *Nano Lett.*, 2020, **20**, 5001–5007.
31 B. Fleury, M.-A. Neouze, J.-M. Guigner, N. Menguy, O. Spalla, T. Gacoin and D. Carriere, *ACS Nano*, 2014, **8**, 2602–2608.
32 A. P. Freitas, R. K. Ramamoorthy, M. Durelle, E. Larquet, I. Maurin, F. Testard, C. Chevallard, T. Gacoin and D. Carriere, *Nano Lett.*, 2021, **22**, 29–35.
33 J. Raimbault, C. Chevallard, D. Ihiawakrim, V. Ramnarain, O. Ersen, F. Gobeaux and D. Carriere, *Nano Lett.*, 2025, **25**, 2275–2282.
34 F. Pschunder, J. Puig, L. J. Giovanetti, C. Huck-Iriart, F. G. Requejo, D. Buceta, C. E. Hoppe and J. M. Ramallo-López, *J. Phys. Chem. C*, 2018, **122**, 29051–29061.
35 K. Ramamoorthy, E. Yildirim, E. Barba, P. Roblin, J. A. Vargas, L.-M. Lacroix, I. Rodriguez-Ruiz, P. Decorse, V. Petkov, S. Teychené and G. Viau, *Nanoscale*, 2020, **12**, 16173–16188.
36 Y. Huang, Z. Wang, X. Chen, C. Luan and K. Yu, *J. Phys. Chem. Lett.*, 2025, **16**, 5398–5404.
37 B. Abécassis, F. Testard, O. Spalla and P. Barboux, *Nano Lett.*, 2007, **7**, 1723–1727.
38 X. Chen, J. Schröder, S. Hauschild, S. Rosenfeldt, M. Dulle and S. Förster, *Langmuir*, 2015, **31**, 11678–11691.
39 T. Li, A. J. Senesi and B. Lee, *Chem. Rev.*, 2016, **116**, 11128–11180.
40 T. Narayanan, *Adv. Colloid Interface Sci.*, 2024, **325**, 103114.
41 C. B. Whitehead and R. G. Finke, *Mater. Adv.*, 2021, **2**, 6532–6568.
42 R. K. Ramamoorthy, E. Yildirim, I. Rodríguez-Ruiz, P. Roblin, L.-M. Lacroix, A. Diaz, R. Parmar, S. Teychené and G. Viau, *Lab Chip*, 2024, **24**, 327–338.
43 S. Nath, S. Jana, M. Pradhan and T. Pal, *J. Colloid Interface Sci.*, 2010, **341**, 333–352.
44 S. Mozaffari, W. Li, M. Dixit, S. Seifert, B. Lee, L. Kovarik, G. Mpourmpakis and A. M. Karim, *Nanoscale Adv.*, 2019, **1**, 4052–4066.
45 B. Abécassis, M. W. Greenberg, V. Bal, B. M. McMurtry, M. P. Campos, L. Guillemeney, B. Mahler, S. Prevost, L. Sharpnack, M. P. Hendricks, D. DeRosha, E. Bennett, N. Saenz, B. Peters and J. S. Owen, *Chem. Sci.*, 2022, **13**, 4977.
46 P. T. Prins, F. Montanarella, K. Dümbgen, Y. Justo, J. C. van der Bok, S. O. M. Hinterding, J. J. Geuchies, J. Maes, K. De Nolf, S. Deelen, H. Meijer, T. Zinn, A. V. Petukhov, F. T. Rabouw, C. De Mello Donega, D. Vanmaekelbergh and Z. Hens, *Nano Lett.*, 2021, **21**, 2487–2496.
47 X. Yin, M. Shi, J. Wu, Y. T. Pan, D. L. Gray, J. A. Bertke and H. Yang, *Nano Lett.*, 2017, **17**, 6146–6150.
48 J. De Roo, *Chem. Mater.*, 2022, **34**, 5766–5779.
49 H. Feng, Y. Yang, Y. You, G. Li, J. Guo, T. Yu, Z. Shen, T. Wu and B. Xing, *Chem. Commun.*, 2009, 1984–1986.
50 A. Loubat, L.-M. Lacroix, A. Robert, M. Impéror-Clerc, R. Poteau, L. Maron, R. Arenal, B. Pansu and G. Viau, *J. Phys. Chem. C*, 2015, **119**, 4422–4430.
51 A. Sugie, T. Somete, K. Kanie, A. Muramatsu and A. Mori, *Chem. Commun.*, 2008, **33**, 3882–3884.
52 R. Parmar, R. K. Ramamoorthy, P. Roblin, N. Ratel-Ramond, L.-M. Lacroix, I. Rodriguez-Ruiz, S. Teychené and G. Viau, *Chem. Mater.*, 2025, **37**, 3423–3433.

53 F. Cui, Y. Yu, L. Dou, J. Sun, Q. Yang, C. Schildknecht, K. Schierle-Arndt and P. Yang, *Nano Lett.*, 2015, **15**, 7610–7615.
54 J. M. Rahm and P. Erhart, *Nano Lett.*, 2017, **17**, 5775–5781.
55 A. S. Mule, S. Mazzotti, A. A. Rossinelli, M. Aellen, P. T. Prins, J. C. van der Bok, S. F. Solari, Y. M. Glauser, P. V. Kumar, A. Riedinger and D. J. Norris, *J. Am. Chem. Soc.*, 2021, **143**, 2037–2048.
56 D. Nelli, C. Roncaglia, R. Ferrando, Z. Kataya, Y. Garreau, A. Coati, C. Andreazza-Vignolle and P. Andreazza, *Nanoscale*, 2023, **15**, 18891–18900.
57 P. J. Chupas, K. W. Chapman, G. Jennings, P. L. Lee and C. P. Grey, *J. Am. Chem. Soc.*, 2007, **129**, 13822.
58 X. Chen, J. Wang, R. Pan, S. Roth and S. Förster, *J. Phys. Chem. C*, 2021, **125**, 1087–1095.